Acta Biomaterialia 6 (2010) 1763–1771

Contents lists available at ScienceDirect

Acta Biomaterialia

journal homepage: www.elsevier.com/locate/actabiomat

Corrosion behaviour of AZ31 magnesium alloy with different grain sizes in simulated biological fluids ☆

M. Alvarez-Lopez [a], María Dolores Pereda [b,c], J.A. del Valle [a], M. Fernandez-Lorenzo [b,c], M.C. Garcia-Alonso [a], O.A. Ruano [a], M.L. Escudero [a,*]

[a] Centro Nacional de Investigaciones Metalúrgicas, CENIM, Consejo Superior de Investigaciones Científicas, CSIC, Avda. Gregorio del Amo 8, 28040 Madrid, Spain
[b] Instituto de Investigaciones Fisicoquímicas Teóricas y Aplicadas (INIFTA), Facultad de Ciencias Exactas, Universidad Nacional de La Plata—CONICET, Casilla de Correo 16, Sucursal 4, 1900 La Plata, Argentina
[c] Facultad de Ingeniería, Calle 1 esq. 47, Universidad Nacional de La Plata, 1900 La Plata, Argentina

ARTICLE INFO

Article history:
Received 4 February 2009
Received in revised form 24 April 2009
Accepted 28 April 2009
Available online 13 May 2009

Keywords:
AZ31 Mg alloy
Grain size
Biomaterial
Corrosion
Electrochemical techniques

ABSTRACT

The corrosion behaviour of AZ31 magnesium alloy with different grain sizes immersed in simulated body fluids was compared in chloride solution (8 g l^{-1}) and in phosphate-buffer solution (PBS). The influence of immersion time was also analyzed. Electrochemical techniques such as open circuit potential, polarization curves, transient currents and electrochemical impedance spectroscopy, complemented with scanning electron microscopy and energy dispersive spectroscopy, were used. Immediately after the immersion in the corrosive media the corrosion resistance was similar for both grain sizes of the AZ31 alloy and higher in NaCl solutions than in PBS. However, this corrosion behaviour was reversed after longer periods of immersion due to the stabilizing of the corrosion products of MgO by P-containing compounds. These P-compounds contribute to a higher level of protection by hindering the aggressive action of chloride ions. The best corrosion behaviour of the AZ31 alloy was obtained for the finest grain alloy associated with the highest transfer resistance value, after long periods of immersion in PBS.

1. Introduction

Magnesium is present in high concentrations in sea water and is the eighth most abundant element on Earth. It has also excellent specific strength and low density, only two-thirds that of Al, so Mg and its alloys can be used in many applications including computer parts, mobile phones, aerospace components, handheld tools, etc. [1,2]. Mg alloys are also potentially useful for bone implants and stent applications due to their low density, inherent biocompatibility and adequate mechanical properties, including a fracture toughness higher than that of ceramics [3–6]. Additionally, the elastic modulus of Mg alloys (40–45 GPa) is closer to that of human bones (10–40 GPa) than other commonly used implant materials. As a result, the stress-shielding phenomena caused by current metallic implants made of stainless steel or Ti alloy can be minimized [7].

Another advantage of Mg in relation to other metallic implants is the degradability of Mg alloys which offers the possibility of better physiological repair and better reconstruction of vascular compliance with minimum inflammatory response [8]. It has been shown that magnesium apatite precipitates on the surface of the modified pure Mg [9,10] and osteoblasts respond by degrading Mg alloys in guinea pig femur [11]. Mg alloys have also shown osteoconductive and osteoinductive properties, thus offering a less invasive repair and temporary support during tissue recovery [7]. The alloys are gradually dissolved or absorbed by the body. In this regard, they are superior to permanent implants, which may cause mismatches in behaviour between the implant and the body as well as physical irritation and chronic inflammatory reactions. As degradable materials, they will not remain as permanent implants in the body and will not require a second surgical operation after the tissue is repaired. Evaluation of the cytotoxicity of Mg and its alloys is reported in Ref. [12].

The major drawback of Mg alloys is that they tend to corrode very quickly in the physiological pH (7.4–7.6) environment, thereby losing their mechanical integrity before the end of the period necessary for bone tissue healing. Therefore, the promising future of Mg and its alloys is dependent on being able to control the rate of corrosion in body fluids.

Several treatments to protect Mg against corrosion have been proposed, such as Mg purification [13], fluoride conversion coatings [14], alloying with other elements and anodizing [1,13,15]. Several studies [16–22] have shown that the corrosion behaviour

☆ Part of Thermec'2009 Biodegradable Metals Special Issue, edited by Professor Diego Mantovani and Professor Frank Witte.

* Corresponding author. Tel.: +34 91 5538900x247; fax: +34 91 5347425.
E-mail address: escudero@cenim.csic.es (M.L. Escudero).

1742-7061/$ - see front matter © 2009 Acta Materialia Inc. All rights reserved.
doi:10.1016/j.actbio.2009.04.041

of Mg alloys is significantly dependent on the microstructure and particularly on the amount and distribution of the intermetallic phases and the grain size. Attempts at improving the corrosion resistance of Mg alloys by their reducing grain size have been proposed by means of laser fusion technology. However, the results obtained by various authors are contradictory [23,24]. Microcrystallization has been also proposed as a way to improve resistance in chloride media [25].

It can therefore be concluded that the reduction of the corrosion rate, by grain size refinement, and the changes in this rate as a function of the physiological media is not well established in the case of Mg alloys. The aim of this work is to evaluate these two effects in an attempt to develop a Mg alloy with improved corrosion resistance.

2. Materials and methods

2.1. Materials

The AZ31 alloy was received from Magnesium Elektron in the form of a rolled 3 mm thick sheet in the O-temper condition (annealed at 345 °C) and also in the form of a cast ingot. The chemical composition of both types of AZ31 alloy was determined by wavelength dispersion X-ray fluorescence (WDXRF) to be: 3.41 ± 0.09 wt.% Al, 0.841 ± 0.039 wt.% Zn, 0.176 ± 0.013 wt.% Mn (balance Mg). The alloy was solution heat-treated at 450 °C for 30 min and water quenched. Rolled sheet disks of 10 mm in diameter were spark machined; these samples were termed type I.

Slabs, machined from the ingot, were processed by equal-channel angular pressing (ECAP). The first pass was made at 250 °C using a square die 12 mm × 12 mm, with an intersection angle of $\Phi = 90°$ and a plunger speed of 0.1 mm s^{-1} [26]. The die was heated in situ during the ECAP process and the temperature of the die was maintained stable. The samples were heated successively to 300 °C and rolled by applying a reduction in thickness from 12 mm to a final thickness of 3 mm in one rolling pass. Rapid cooling (quenching) took place during rolling, since the rolling mill was at room temperature. Disks 10 mm in diameter were machined from the rolled slabs; these samples are termed type II.

2.2. Microstructural characterization

The microstructures of the alloy in the different stages of processing were examined by optical microscopy (OM). The sample preparation consisted of grinding on SiC paper, followed by mechanical polishing with 6 and 1 μm diamond paste and short final polishing using colloidal silica. The grain structure was revealed by subsequent etching using a solution of ethanol (100 ml), picric acid (5 g), acetic acid (5 ml) and water (10 ml).

Microstructural and compositional characterization of the alloy surface was carried out by scanning electron microscopy (SEM) and energy-dispersive X-ray spectroscopy (EDX) microanalysis, after immersion tests in the corrosive media. Fourier transform infrared (FTIR) spectroscopy from 4000 to 400 cm^{-1} was also performed to identify the functional groups in the corrosion products.

2.3. Corrosive media and electrochemical techniques

The following solutions were used as electrolytes: (i) 8.00 g l^{-1} NaCl solution; and (ii) phosphate-buffer solution (PBS), comprising 0.20 g l^{-1} KCl, 0.20 g l^{-1} KH_2PO_4, 8.00 g l^{-1} NaCl and 1.15 g l^{-1} Na_2HPO_4 (anhydrous).

A conventional three-electrode electrochemical cell with a platinum wire as a counter-electrode and Ag/AgCl as a reference electrode was used. The working electrodes were the AZ31 disks. The surface was ground with SiC abrasive paper of increasing grain size from 600 to 1200 in water and finally polished with 1 μm diamond suspension. Finally, AZ31 samples were rinsed ultrasonically in ethanol. Single sweep potentiodynamic polarization curves were performed at 37 °C at 10 mV s^{-1}, between −1.88 $V_{vs.Ag/AgCl}$ and different anodic limits. The passivation currents and breakdown potentials (E_{bd}) were determined. At least five polarization curves were generated for each condition (types I and II in PBS and NaCl solutions). Transient currents were recorded at −1.54 V after a potential step between −1.88 $V_{vs.Ag/AgCl}$ and −1.54 $V_{vs.Ag/AgCl}$.

Electrochemical impedance spectroscopy (EIS) was carried out after 2 h, 24 h and 2, 3, 4 and 6 days testing time. Before the EIS measurements, the corrosion potential was registered over 10 min until the potential was stabilised. The EIS experiments were performed at the corrosion potential by applying a sinusoidal wave of 10 mV in amplitude over a frequency range from 2×10^4 to 10^{-2} Hz spaced logarithmically (five per decade). A 1280 Solartron frequency response analyzer was used to perform the electrochemical tests.

The EIS results were analyzed by fitting the experimental impedance data with different equivalent circuit models. The equivalent circuit parameters were calculated by fitting the impedance function to the measured spectra by a non-linear least-squares program for all the frequencies measured. The criteria used in estimating the quality of the fitting were evaluated firstly with the lower χ^2 value, and secondly with the lower estimative errors (in per cent) for all the components.

3. Results

3.1. Microstructural characterization

The microstructures of type I and type II AZ31 alloy are shown in Fig. 1a and b, respectively. True grain sizes were measured by the linear intercept method using a correction factor of 1.74. The mean grain sizes were $d = 25.7$ and 4.5 μm for type I and type II samples, respectively. In both type I and type II samples, some particles of Mn-rich phase (Al_6Mn) still remained in the microstructure after processing. Their volume fraction was estimated by image analysis to be close to 3×10^{-3}.

3.2. Initial stages of corrosion

Polarization curves recorded immediately after the immersion of type I and type II AZ31 samples in NaCl and PBS are shown in Fig. 2a and b, respectively. Higher cathodic current and slightly higher breakdown potential is observed for the NaCl than for the PBS solutions. The breakdown potential measured in both solutions is similar for these samples. The influence of albumin protein on the corrosion behaviour was also considered. Results are not shown since slight shifts were observed in the polarization curves for type I and type II samples in both 1 and 10 g l^{-1} albumin-containing PBS with respect to the PBS control without albumin.

The transient current recorded at −1.54 $V_{vs.Ag/AgCl}$ in NaCl and PBS solutions for type I and type II AZ31 alloy is shown in Fig. 3a and b, respectively. In the case of NaCl solution, the figures initially reveal that the current decreases, remains stable for a few seconds and then increases rapidly. Conversely, in the case of PBS, after the initial decrease, the current increases immediately for both type I and type II AZ31 alloy.

Fig. 4 shows the Nyquist impedance plots for type I (Fig. 4a and b) and type II (Fig. 4c and d) samples after 2, 24 and 48 h of immersion in NaCl and PBS, respectively. In these plots a depressed semicircle at high and medium frequencies is observed for all immersion times, independent of the medium. The AZ31 samples

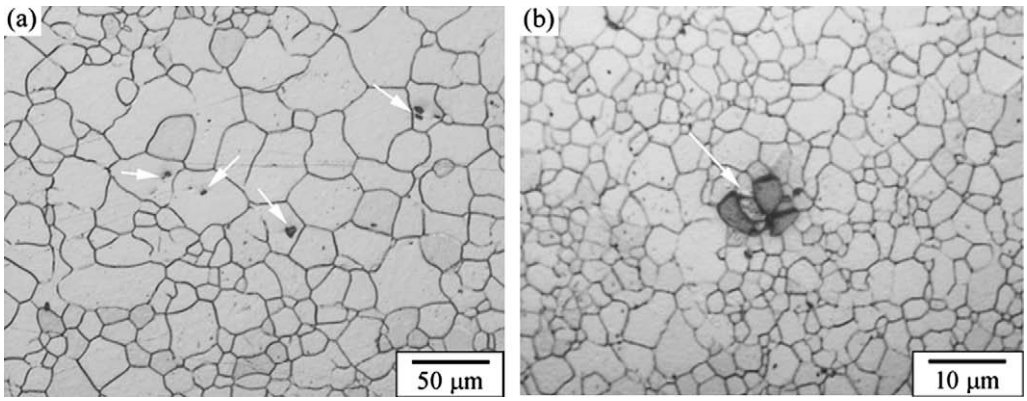

Fig. 1. Microstructure of AZ31 samples, type I (a) and type II (b), and some particles of Mn-rich phase (Al_6Mn) present in both types of samples.

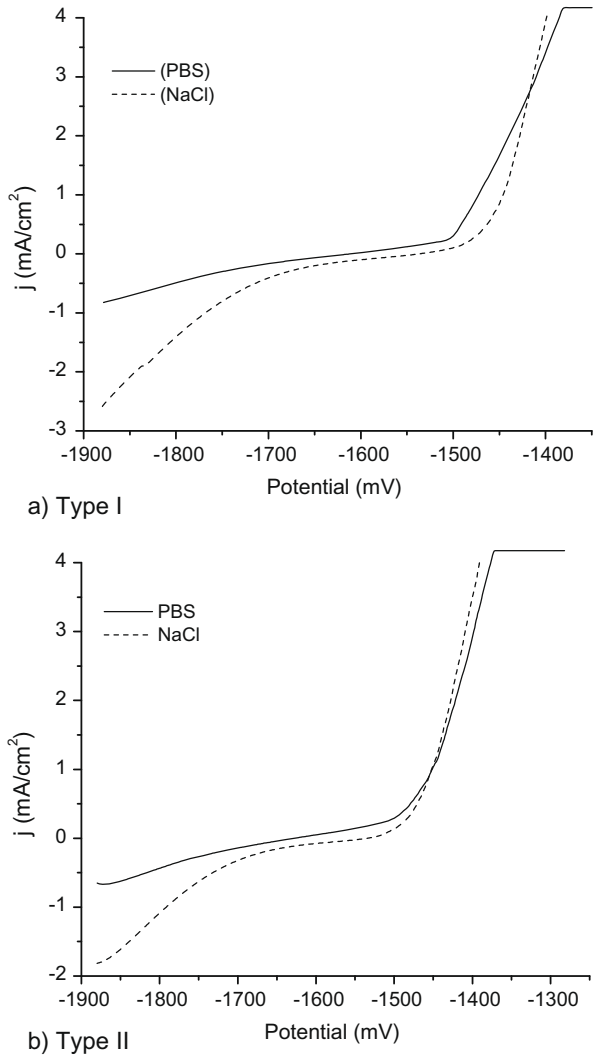

Fig. 2. Representative potentiodynamic polarization curves of type I (a) and type II (b) AZ31 alloy at 10 mV s^{-1} in NaCl and PBS. The number of experimental curves obtained for each condition is $n = 5$.

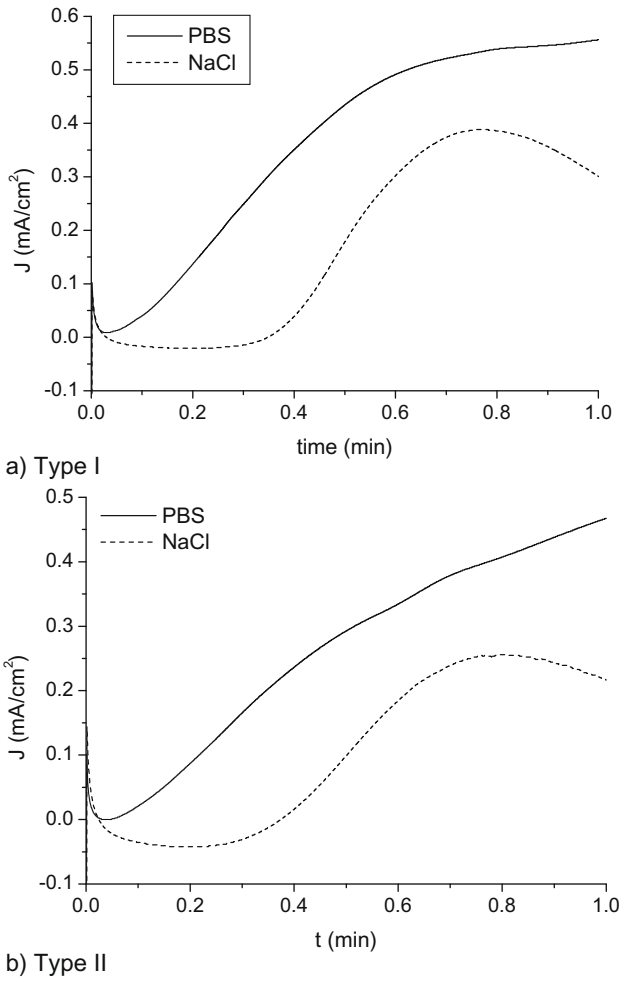

Fig. 3. Transient currents recorded at $-1.54\ V_{(Ag/AgCl)}$ in type I (a) and type II (b) AZ31 alloy in NaCl and PBS.

show an inductive loop at low frequencies in all cases (Fig. 4a–c), except for type II samples immersed in PBS (Fig. 4d). Considering that the kinetics of the corrosion behaviour is estimated from the capacitive arc obtained in the high-frequency (HF) and medium-frequency (MF) ranges, the analysis of the impedance data will focus on this part of the spectra. By comparing the diameter of the capacitive arcs at initial immersion times (2 h), obtained in Fig. 4, higher diameters for samples immersed in NaCl than those immersed in PBS were found, thus showing a higher corrosion resistance in NaCl medium. However, the evolution of immersion time over the first 48 h does not produce significant changes of the diameter in the first semicircle, except for type II samples immersed in PBS, in which the diameter is higher.

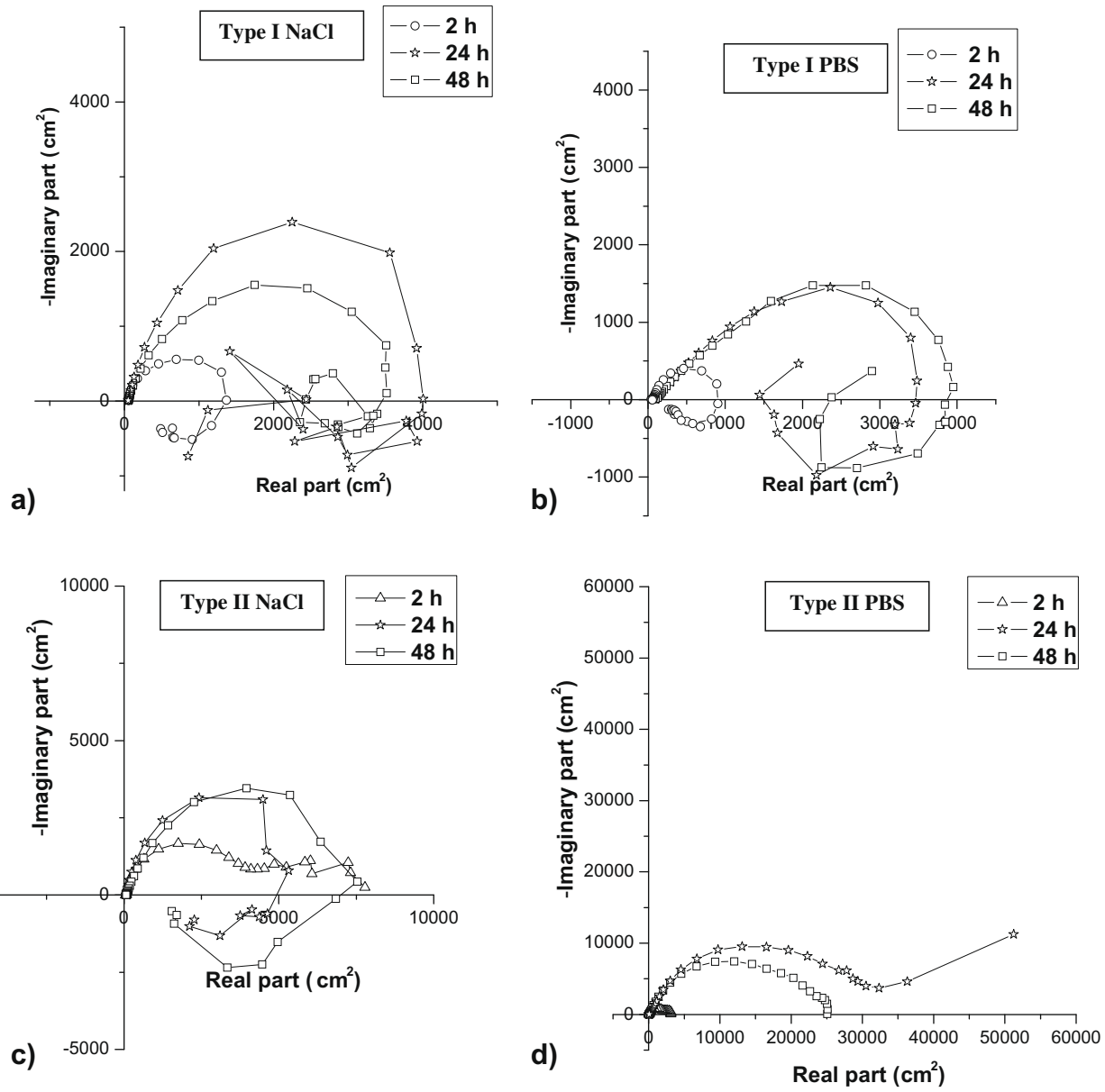

Fig. 4. Nyquist plots of type I AZ31 alloy in NaCl (a) and PBS (b) and type II AZ31 alloy in NaCl (c) and PBS (d) after 2, 24 and 48 h of immersion.

This fact is corroborated by the examination of the surface by optical and electron microscopy. Fig. 5 shows micrographs of the formation of a pit after 30 min immersion in PBS for type II samples. The optical micrograph (Fig. 5a) shows that the surface is covered by a dark protective layer with white circles inside. Fig. 5b shows a pit, around which precipitation has taken place. The mapping of the elements detected in this area can be seen in Fig. 5c–j. The small pit is formed close to the intermetallic AlMn deposit (Fig. 5b, d and e). High P signals around the pits are observed in Fig. 5g. However, after 1 h immersion, type II samples did not show any pit formation in NaCl. This observation indicates that the phosphate included in the PBS initially accelerates the corrosion of the AZ31 alloy.

3.3. Evolution over time of the corrosion kinetics

Fig. 6a and b shows the impedance plots for type I and type II in NaCl and PBS solutions after immersion for 6 days. A higher diameter for type II samples is obtained, irrespective of the medium. For this type II, the semicircle diameter is higher when samples are immersed in PBS. With respect to type I AZ31 samples, the magnitude of the semicircle is practically the same, irrespective of the medium used.

Analysis of experimental impedance data shows that more than one time constant is necessary to describe the corrosion behaviour since the impedance data do not produce a simple semicircle in the capacitive half plane. Fig. 7 shows the equivalent circuits used to simulate the impedance data of the AZ31 alloy of both types of samples, I and II, immersed in NaCl or PBS solutions. The HF–MF arc was simulated by using a simple Randles circuit (Fig. 7a) consisting of the electrolyte resistance (Rs), in series with a constant phase element (CPE) simulating a non-ideal behaviour of the capacitor due to the sum of the oxide layer capacitance and the double-layer capacitance, in parallel with the transfer charge resistance (R1). In order to simulate the low-frequency (LF) range, a second branch is added in the Randles circuit (Fig. 7b), in which an inductive element L1 appears to describe the corrosion behaviour at low frequencies. The fitting of the first arc (HF–MF range) gives

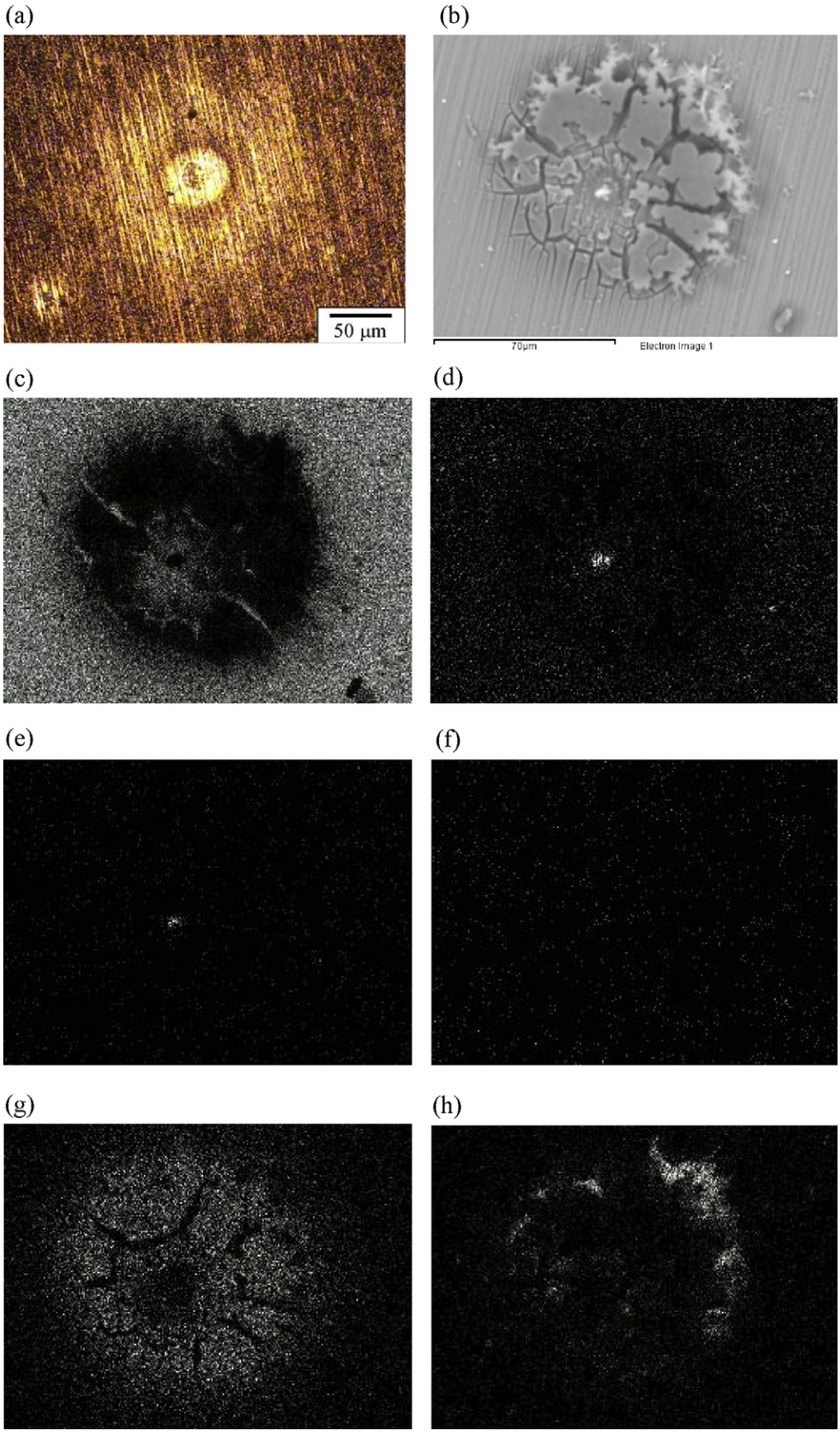

Fig. 5. Micrographs of the formation of a small pit after 30 min of immersion for type II AZ31 alloy in PBS: (a) optical microscopy, (b) SEM image, (c) mapping of Mg, (d) mapping of Al, (e) mapping of Mn, (f) mapping of Fe, (g) mapping of P, (h) mapping of Cl, (i) mapping of Na and (j) mapping of O.

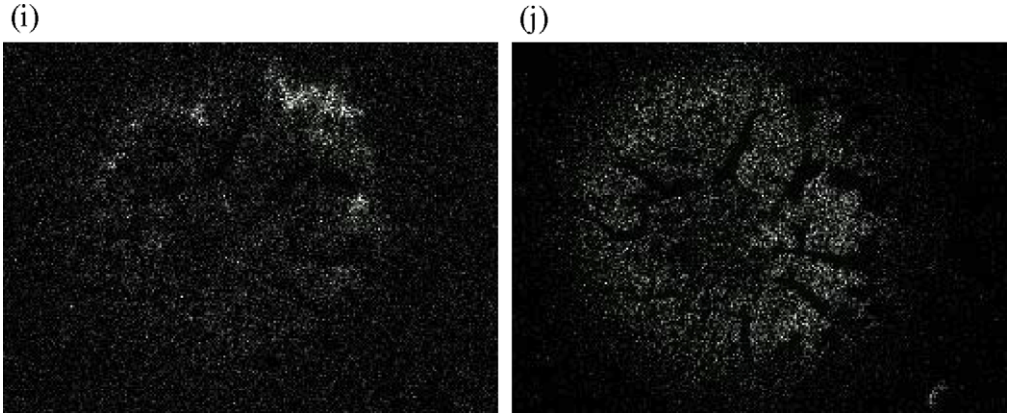

Fig. 5 (*continued*)

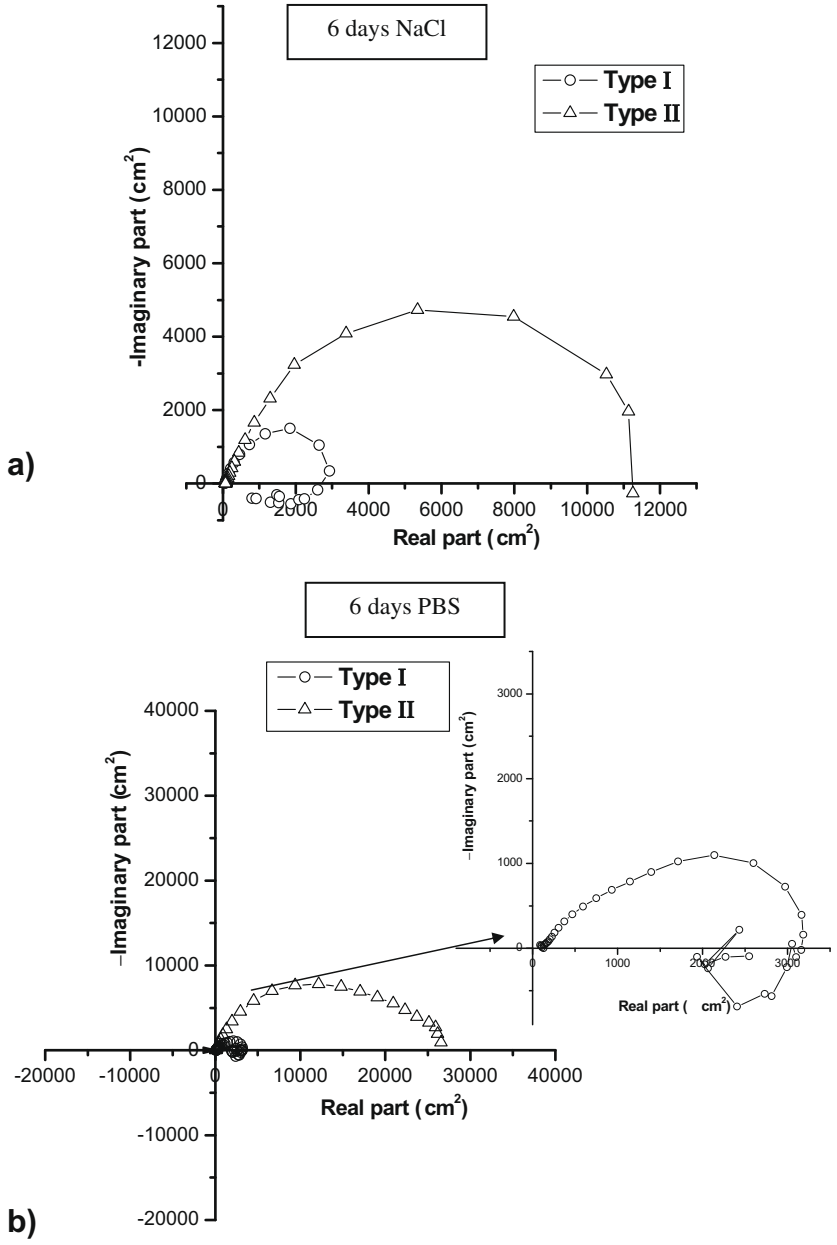

Fig. 6. Nyquist plots of type I and type II AZ31 alloys immersed in (a) NaCl or (b) PBS solutions for 6 days.

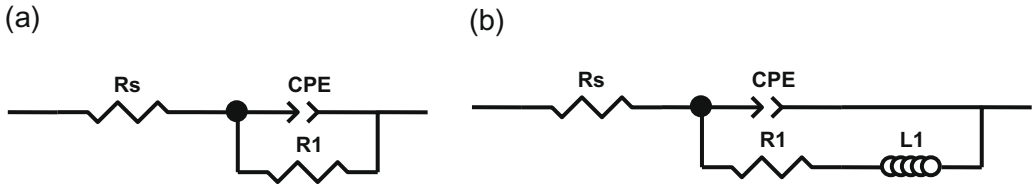

Fig. 7. Equivalent circuits. Rs is the electrolyte resistance; CPE1 is the oxide film capacitance and the double-layer capacitance; R1 is the charge transfer resistance and the oxide film resistance; L1 is the inductive element.

valuable information about the corrosion kinetics of the AZ31 alloy. Table 1 shows fitting values obtained with the equivalent circuits and experimental values obtained from the impedance data. Table 1 summarizes the values obtained for type I and type II, in both corrosive media at 2 h and after 6 days immersion. The increase in Rs over time is higher in PBS than in NaCl solutions, irrespective of the type of sample. In addition, an improvement in R1 over time for type I samples immersed in NaCl and PBS solutions is seen. The same is observed in type II samples but the effect is more pronounced in PBS. On the other hand, type II samples immersed in NaCl show that the capacitance slightly increases, whereas in PBS the capacitance is nearly constant.

The corrosion products of AZ31 samples immersed for 6 days in PBS medium were analyzed by FTIR. As an example, Fig. 8 shows the spectrum acquired from AZ31 samples. The broad absorption band from 3700 to 2500 cm^{-1} is attributed to the vibration of water molecules. The band at 1650 cm^{-1} is also attributed to water vibration. The absorption bands at 992 and 422 cm^{-1} correspond to phosphate $(PO_4)^{3-}$. Finally, the band at 823 cm^{-1} is assigned to the Mg–O bonding vibration.

Table 1
Results obtained from the impedance diagrams for the type I and type II AZ31 alloys in NaCl and PBS over immersion time and fitted data of the equivalents circuits of Fig. 7.

Material	Medium	Time	Condition	Rs (Ω)	C (μF cm^{-2} CPE)	R1 (Ω cm^2)
Type I	NaCl	2 h	Experimental	109	7.8	1268
			Fitting	109	10.8	1211
		6 days	Experimental	135	10.0	3838
			Fitting	130	21.2	4021
	PBS	2 h	Experimental	113	12.6	885
			Fitting	113	18.8	922
		6 days	Experimental	261	1.6	2230
			Fitting	268	34.0	2847
Type II	NaCl	2 h	Experimental	150	7.6	3860
			Fitting	148	9.2	3706
		6 days	Experimental	166	14.4	12,400
			Fitting	166	24.0	13,330
	PBS	2 h	Experimental	113	11.4	2139
			Fitting	114	21.2	2299
		6 days	Experimental	179	14.3	22,558
			Fitting	171	19.6	22,959

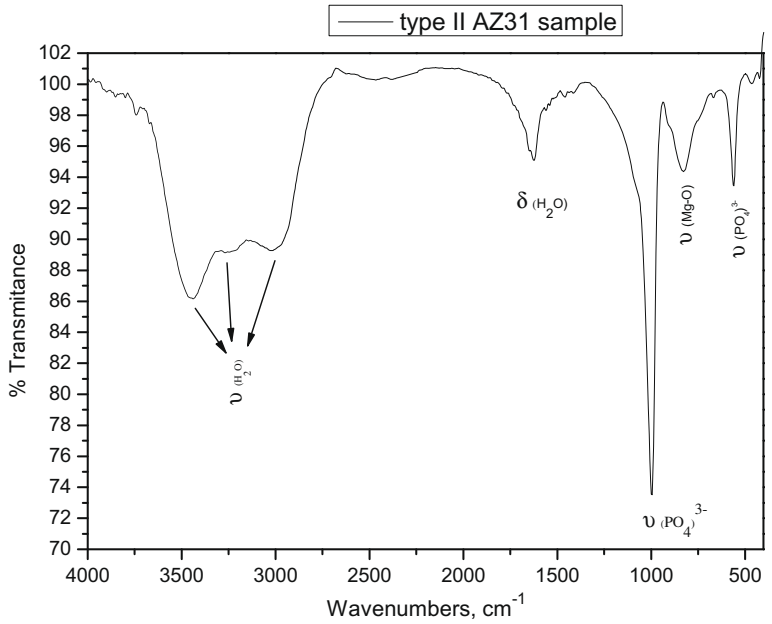

Fig. 8. FTIR spectrum of corrosion products of type II AZ31 samples immersed in PBS for 6 days.

4. Discussion

The application of Mg and its alloys as biomaterial for temporary implants in the form of plates and screws would be effective if the corrosion kinetics could be understood and controlled in body fluids. A possible route to reduce the corrosion rate could be the reduction of the grain size. With this goal in sight, the research developed in this work consisted mainly of the evaluation of the corrosion behaviour of type I and type II AZ31 Mg alloy of different grain sizes in two electrolyte media. The Al present in the AZ31 alloy, 3 wt.%, increases the corrosion resistance of Mg by stabilizing the passive layer [16,27–28]. Larger amounts of Al are not recommended since aluminium ions can easily combine with inorganic phosphates, leading to a lack of phosphate in the human body and inducing dementia [13,29]. Furthermore, the relatively small amount of Al ensures the presence of only one phase in the alloy, thus avoiding second phases that may be detrimental to the corrosion behaviour. The Zn content in the alloy results in satisfactory mechanical properties and can, at the same time, be tolerated in the human body [30]. Hence this Zn content increases the corrosion resistance and retards the biodegradation of Mg alloys [13,16].

Type I AZ31 samples are in the O-temper condition, i.e., they have an annealed and recrystallized microstructure. The processing route used to obtain type II samples leads to a fine grain size, 4.5 μm, which is similar to that obtained with severe plastic deformation techniques. The processing temperature of the rolling pass, 300 °C, is above the solvus temperature for Al in this alloy. Therefore, the Al is in solid solution during rolling. Due to the rapid cooling that takes place after rolling and since the rolling mill is at room temperature, no precipitation of the β-phase, $Mg_{17}Al_{12}$, takes place. Compositional maps obtained by EDX show that Zn and Al are homogeneously distributed in the Mg matrix in both type I and type II samples. After the processing route [31], some particles of Mn-rich phase (Al_6Mn) still remain in the microstructure as can be seen in Fig. 5.

Results for the initial stages of immersion show that the corrosion behaviour of type I and type II samples depends on the testing media, NaCl or PBS. The polarization curves obtained in 8 g l^{-1} NaCl (Fig. 2) show a pseudo-passive region followed by a sharp current increase at the breakdown potential due to the action of chloride. Correspondingly, the current transients for type II (Fig. 3) and type I recorded at -1.54 $V_{vs.Ag/AgCl}$ in NaCl show that the current decreases initially, probably due to the formation of the pseudopassive layer of $Mg(OH)_2$. The current remains low during 20 s for type I and type II in NaCl and then increases due to the localized corrosion induced by chloride ions. Pitting subsequently spreads laterally. The current "plateau" is not observed in PBS. In this case, the current increases immediately because the high pH needed for $Mg(OH)_2$ formation is not reached. In the same way, after a short immersion period (30 min) pits are only observed in PBS. These results agree with the transfer resistance, R1 values (Table 1 at 2 h.) obtained from impedance diagrams (Fig. 4), which show a higher value in NaCl than in PBS. This different behaviour is attributed to the electrochemical dissolution of Mg in the surrounding areas (anodic zones) of the intermetallic inclusions (cathodic areas).

The kinetics data of the corrosion behaviour of the samples are shown in Table 1, and summarize the charge transfer resistance (R1) values obtained from the HF–MF capacitive arc at 2 h testing. The diameter of the first capacitive arc at high frequency (Fig. 4) can be ascribed to the R1 value, which includes the resistance of the passive film and/or the layer of corrosion products [32]. The diameter of the semicircle closely corresponds to the R1 value only if the resistance of the passive film is much lower than the charge transfer resistance [32]. The capacitance values obtained for the largest semicircles are 7.8 and 12.6 μF cm^{-2} in NaCl and PBS, respectively, for the type I samples (similar values are also obtained for type II samples). These values are lower than those obtained for the electrochemical double layer which are about 20–50 μF cm^{-2} [32].

The best electrochemical results at the initial stages, obtained in samples immersed in NaCl solution with respect to the PBS medium, can be attributed to the electrochemical dissolution of Mg, thus favouring the production of OH^- ions as a result of hydrogen gas formation from the cathodic reaction. The presence of OH^- ions causes an increase of pH at the interface and facilitates the formation and precipitation of MgO and/or $Mg(OH)_2$ as corrosion products. In the case of AZ31 samples immersed in PBS, the phosphate ions ($(HPO_4)^{2-}$) may capture the OH^- that is produced by the cathodic reaction and consequently the highly alkaline pH that favours the massive precipitation of Mg hydroxide cannot be attained. On the other hand, the phosphate precipitation hinders the action of chloride, and Mg dissolution is slower.

The change of corrosion potential, E_{corr}, over time (Fig. 9) is more important in type II and is probably related to its higher surface reactivity being more evident during the first hours. The most marked differences between type I and type II samples could be observed in the EIS measurements. After the first capacitive arc that appears in both samples (Fig. 4), the shape of the impedance diagrams is different. The type I samples immersed in both media and type II samples in NaCl solution show an inductive arc (Fig. 4a and b). However, type II samples in PBS show a possible second arc or a straight line associated with a diffusion process (Fig. 4c and d).

The inductive loop (type I) is assumed to be due to the formation of the $Mg(OH)_2$ and/or MgO, already mentioned, and to the coverage due to an adsorbed intermediate (probably $Mg(OH)^+_{ads}$) or $Mg(OH)_2$ [14,29]. The presence of this loop has been attributed to pitting processes [33] and also to the formation and precipitation of a salt film [34]. In our case, a discrete thin film is formed in the air and pitting corrosion may easily be initiated in the presence of chloride ions. It is the dissolution of this film that yields the formation of corrosion products on the electrode surface. This behaviour agrees with the observation of other authors on the same alloy, AZ31, immersed in 3.0 wt.% NaCl [1,35].

The second arc observed for type II samples (Fig. 4c and d) in PBS medium could be attributed to mass transport in the solid phase due to the growth of the corrosion product layer [16], facilitated by the finer grain size. In our case, the corrosion products are basically formed by MgO and $(PO_4)^{3-}$ (Fig. 8). This diffusion process

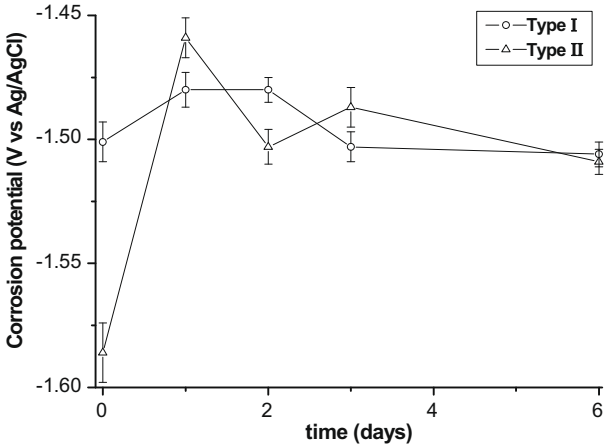

Fig. 9. Change in corrosion potential, E_{corr}, of type I and type II AZ31 alloy in PBS with immersion time.

slows down the corrosion reaction, giving rise to an increase in the corrosion resistance, i.e., to a decrease in the corrosion rate.

The corrosion behaviour at initial stages is reversed when immersion time is increased, and after 6 days the corrosion resistance is improved. R1 increases its value for samples immersed in PBS with respect to those immersed in NaCl solution (Table 1). This evolution of the corrosion behaviour with immersion time is due to the accumulation of corrosion products, forming a layer that promotes diffusive control of the corrosion process of the samples. After 6 days testing in PBS, the released $(PO_4)^{3-}$ has co-precipitated together with the MgO as shown in our FTIR results (Fig. 8), which agree with those of other authors [36]. The increase in R1 over time could be related to the formation of a mixed layer that is increasingly thick and more compact with time, hindering the diffusion of ions, particularly in case of type II.

In summary, the best corrosion behaviour of the AZ31 is obtained for the finest grain alloy, type II, with respect to the coarser one. This good result is attributed to a more negative corrosion potential giving rise to a fast electrochemical reaction and the formation of a layer of corrosion products, which offers more protection from the diffusion of aggressive ions to the electrode surface than found with type I. Immediately after immersion, the corrosion resistance is higher in NaCl solution than in PBS, but this behaviour is reversed after longer periods of immersion due to the stabilization of the layer by P-containing compounds. These compounds contribute to a higher protection than that of the magnesium hydroxide formed in NaCl solution because they hinder the detrimental action of chloride ions.

5. Conclusions

1. At initial stages, pits are associated with the presence of AlMn intermetallics. The monophasic AZ31 alloy shows pitting corrosion that spreads laterally for both types of samples.
2. For short periods, the initiation of localized corrosion occurs earlier in PBS than in NaCl. However, the precipitation of P-containing salts in PBS decreases the corrosion rate over time for both types of samples.
3. The best corrosion behaviour corresponds to the AZ31 alloy with the finest grain size in PBS. It reveals the lower initial corrosion potential and higher charge transfer resistance values at long immersion periods. This could be related to the presence of a mixed compact layer of P-containing compounds, together with magnesium hydroxide, that promote protection against the action of chloride ions.

Acknowledgements

The authors acknowledge the Ministerio de Educación y Ciencia, Spain, for financial support by projects MAT 2006-02672 and MAT2008-06719-C03-01.

D.P. and M.F.L.M. acknowledge the financial support by ANPCyT (PICT 05-33225, PICT 05-32906), UNLP (11/I129) and CONICET (PIP 6075).

References

[1] Wu CS, Zhang Z, Cao FH, Zhang LJ, Zhang JQ, Cao CN. Study on the anodizing of AZ31 magnesium alloys in alkaline borate solutions. Appl Surf Sci 2007;253:3893–8.
[2] Gray JE, Luan B. Protective coatings on magnesium and its alloys—a critical review. J Alloys Compd 2002;336:88–113.
[3] Heublein B, Rohde R, Kaese V, Niemeyer M, Hartung W, Haverich A. Biocorrosion of magnesium alloys: a new principle in cardiovascular implant technology. Heart 2003;89:651–6.
[4] Zartner P, Cesnjevar R, Singer H, Weyand M. First successful implantation of a biodegradable metal stent into the left pulmonary artery of a preterm baby. Catheter Cardio Int 2005;66:590–4.
[5] Staiger M, Pietak A, Huadmai J, Dias G. Magnesium and its alloys as orthopedic biomaterials: a review. Biomaterials 2006;27:1728–34.
[6] Mani G, Feldman MD, Patel D, Agrawal CM. Coronary stents: a materials perspective. Biomaterials 2007;28:1689–710.
[7] Xu L, Yu G, Zhang E, Pan F, Yang K. In vivo corrosion behavior of Mg–Mn–Zn alloy for bone implant application. J Biomed Mater Res A 2007;83A:703–11.
[8] Loos A, Rohde R, Haverich A, Barlach S. In vitro and in vivo biocompatibility testing of absorbable metal stents. Macromol Symp 2007;253:103–8.
[9] Kuwahara H, Al-Abdullat Y, Mazaki N, Tsutsumi S, Aizawa T. Precipitation of magnesium apatite on pure magnesium surface during immersing in Hank's solution. Mater Trans 2001;42:1317–21.
[10] Al-Abdullat Y, Tsutsumi S, Nakajima N, Ohta M, Kuwahara H, Ikeuchi K. Surface modification of magnesium by $NaHCO_3$ and corrosion behaviour in Hank's solution for new biomaterial applications. Mater Trans 2001;42:1777–80.
[11] Witte F, Kaese V, Haferkamp H, Switzer E, Meyer-Linderberg A, Wirth CJ, et al. In vivo corrosion of four magnesium alloys and the associated bone response. Biomaterials 2005;26:3557–63.
[12] Gu X, Zheng Y, Cheng Y, Zhong S, Xi T. In vitro corrosion and biocompatibility of binary magnesium alloys. Biomaterials 2009;30:484–98.
[13] Song G. Control of biodegradation of biocompatible magnesium alloys. Corros Sci 2007;49:1696–701.
[14] Chiu KY, Wong MH, Cheng FT, Man HC. Characterization and corrosion studies of fluoride conversion coating on degradable Mg implants. Surf Coat Technol 2007;202:590–8.
[15] Zhang Y, Yan C, Wang F, Li W. Electrochemical behaviour of anodized Mg alloy AZ91D in chloride containing aqueous solution. Corros Sci 2005;47:2816–31.
[16] Baril G, Blanc C, Pébère N. AC impedance spectroscopy in characterizing time-dependent corrosion of AZ91 and AM50 magnesium alloys. J Electrochem Soc 2001;148:B489–96.
[17] Lunder O, Lein JE, Aune TKr, Nisancioglu K. Role of $Mg_{17}Al_{12}$ phase in the corrosion of Mg alloy AZ91. Corrosion 1989;45:741–8.
[18] Nisancioglu K, Lunder O, Aune TKr. In: Proceedings of the 47th annual world magnesium conference. The International Magnesium Association; 1990. p. 47.
[19] Song G, Atrens A, Wu X, Zhang B. Corrosion behaviour of AZ21, AZ501 and AZ91 in sodium chloride. Corros Sci 1998;40:1769–91.
[20] Song G, Atrens A, Dargusch M. Influence of microstructure on the corrosion of diecast AZ91D. Corros Sci 1999;41:249–73.
[21] Uzan P, Frumin N, Eliezer D, Aghion E. In: Proceedings of the second Israeli international conference on magnesium science and technology; 2000. p. 385–91.
[22] Ambat R, Aung NN, Zhou W. Evaluation of microstructural effects on corrosion behaviour of AZ91D magnesium alloy. Corros Sci 2000;42:1433–55.
[23] Abbas G, Liu Z, Skeldon P. Corrosion behaviour of laser-melted magnesium alloys. Appl Surf Sci 2005;247:347–53.
[24] Dubé D, Fiset M, Couture A, Nakatsugawa I. Characterization and performance of laser melted AZ91D and AM60B. Mat Sci Eng A Struct 2001;299:38–45.
[25] Li Y, Zhang T, Wang F. Effect of microcrystallization on corrosion resistance of AZ91D alloy. Electrochim Acta 2006;51:2845–50.
[26] del Valle JA, Carreño F, Ruano OA. Influence of texture and grain size on work hardening and ductility in magnesium-based alloys processed by ECAP and rolling. Acta Mater 2006;54:4247–59.
[27] Nordlien JH, Nisancioglu K, Ono S, Masuko N. Morphology and structure of oxide films formed on MgAl alloys by exposure to air and water. J Electrochem Soc 1996;143:2564–72.
[28] Nordlien JH, Nisancioglu K, Ono S, Masuko N. Morphology and structure of water-formed oxides on ternary MgAl alloys. J Electrochem Soc 1997;144:461–6.
[29] Lucey TD, Venugopal B. Metal toxicity in mammals. New York: Plenum Press; 1977.
[30] Magos L, Suzuki T. In: Chang L, editor. Toxicology of metals. Boca Raton, FL: CRC Lewis; 1996, ISBN 1-56670-803-6.
[31] Pérez-Prado MT, del Valle JA, Contreras JM, Ruano OA. Microstructural evolution during large strain hot rolling of an AM60 Mg alloy. Scripta Mater 2004;50:661–5.
[32] Pebere N, Riera C, Dabosi F. Investigation of magnesium corrosion in aerated sodium sulfate solution by electrochemical impedance spectroscopy. Electrochim Acta 1990;35:555–61.
[33] Metikoš-Huković M, Babić R, Grubač Z, Brinić S. Impedance spectroscopic study of aluminium and Al-alloys in acid solution: inhibitory action of nitrogen containing compounds. J Appl Electrochem 1994;24:772–8.
[34] Breslin CB, Rudd AL. Activation of pure Al in an indium-containing electrolyte—an electrochemical noise and impedance study. Corros Sci 2000;42:1023–39.
[35] Song G, Atrens A, John D, Wu X, Nairn J. The anodic dissolution of magnesium in chloride and sulphate solutions. Corros Sci 1997;39:1981–2004.
[36] Xin Y, Huo K, Tao H, Tang G, Chu PK. Influence of aggressive ions on the degradation behavior of biomedical magnesium alloy in physiological environment. Acta Biomater 2008;4:2008–15.